Eur. Phys. J. C (2024) 84:988
https://doi.org/10.1140/epjc/s10052-024-13384-3

THE EUROPEAN PHYSICAL JOURNAL C

Regular Article - Theoretical Physics

Circular orbits of accretion flow around charged black hole coupled with a nonlinear electrodynamics field

H. Rehman[1,a] , **G. Abbas**[1,b], **Tao Zhu**[2,3,c] , **Qiang Wu**[2,3,d] , **G. Mustafa**[4,e]

[1] Department of Mathematics, The Islamia University of Bahawalpur, Bahawalpur, Pakistan
[2] Institute for Theoretical Physics and Cosmology, Zhejiang University of Technology, Hangzhou 310032, China
[3] United Center for Gravitational Wave Physics (UCGWP), Zhejiang University of Technology, Hangzhou 310032, China
[4] Department of Physics, Zhejiang Normal University, Jinhua 321004, People's Republic of China

Received: 28 March 2024 / Accepted: 15 September 2024

Abstract This study investigates the particle's geodesic motion and accretion around the spherically symmetric Reissner–Nordström black hole coupled with a nonlinear electrodynamics field. The formation of the disc-like structure in the accretion process arises from the geodesic motion exhibited by particles near the black hole. In the equatorial plane, we analyze the circular orbits of particles and their stability in detail. The analysis of the fluid's critical flow, maximum accretion rate, radiant flux energy, radioactive efficiency, and radiant temperature are also examined near the central object. We analyze the perturbations experienced by particles throughout, employing restoring forces and the oscillatory behavior of the particles around the black hole. Our results show that the NED parameter ζ affects the circular geodesics of particles and the maximum accretion rate of the Reissner–Nordström black hole coupled with nonlinear electrodynamics.

1 Introduction

The theory of general relativity (GR) speculates on the presence of black holes (BHs) as mysterious objects. The extremely strong gravitational field in the universe is considered to have originated from BH. Additionally, it is believed that BHs possess strong magnetic fields and spin. In light of these characteristics, BHs are the ideal astrophysical laboratory for studying the nature of gravity and the matter around it. Based on the examination of observational evidence, empirical data has recently confirmed the existence of BH. The first accomplishment represented the discovery of gravitational waves arising due to the collision of two BHs in a binary system, as observed through the collaborative work of LIGO and Virgo [1]. Another significant role of the Event Horizon Telescope is its utilization of baseline Interferometry to capture the first images of the BH shadow of M87 [2,3], as well as revealed image of Sgr A* [4].

It is believed that cosmic entities, such as BHs, undergo mass accumulation via the phenomenon of accretion. They might also serve to analyze modified theories of gravity. The existence of an accretion disc is an essential element in pursuing the accretion rate encompassing these compact objects. Diffuse matter creates the accretion disc and emits energy by slowly spiraling into a centrally condensed object. Accretion is the process by which a fluid nearby attracts particles to a compact object like a BH. Whenever the fluid velocity is identical to the sound speed, these particles must pass through the critical point. The fluid is projected onto its central mass at supersonic speeds. The BH mass needs to be raised as a result of this event [5]. It is fascinating to analyze numerous usual radii as a consequence of examining the particles' geodesic structure near the BH, such as the innermost stable circular orbit (ISCO) and marginally bound orbit (r_{mb}). In the examination of BH accretion discs, the considered radii are the significant factors.

The ISCO is associated with the inner boundary of the accretion disc around a BH, and their radii can be used to compute the energy emission efficiency, which is a measure of how quickly energy from the rest mass turns into radiation. The locations of unstable or stable circular orbits correspond to the greatest or lowest value of the effective potential, accordingly. According to Newtonian theory, it is

[a] e-mail: hamzarehman244@gmail.com
[b] e-mail: ghulamabbas@iub.edu.pk
[c] e-mail: zhut05@zjut.edu.cn
[d] e-mail: wuq@zjut.edu.cn
[e] e-mail: gmustafa3828@gmail.com (corresponding author)

Published online: 28 September 2024

believed that the ISCO does not have a minimum radius. This is supported by the observation that the ISCO can assume any radius once the effective potential reaches its smallest value for all possible values of angular momentum [6]. For any minimum or maximum value of the angular momentum, the effective potential in GR and particles rotating near the Schwarzschild BH comprises two extremes, so it corresponds with the two points. One can explored ISCO at $r = 3r_g$ [6,7], where r_g denotes the Schwarzschild radius. In [8] and [9], researchers studied the effects of ISCO in the vicinity of Kerr BH and introduced these characteristics in GR.

Thorne and Novikov [10] determined the Kerr and Schwarzschild BH accretion discs efficiency. In [11] Johannsen created the accretion discs around such BHs, while Johannsen and Psaltis [12] presented the Kerr-like metric. The geodesic structure and spherical orbits of charged particles near revolving, weakly magnetic BHs have been identified by Tursunov et al. [13]. Since the particles in the accretion disc revolve in stable orbits, oscillations in the radial, as well as vertical directions with epicyclic frequencies, arise if the particles are perturbed. Because of this, understanding orbital and epicyclic frequencies is important for understanding the mechanisms of the accretion discs that surround BHs. Moreover, the accretion disc and geodesic structure have been analyzed in the literature for various BHs in [14–22].

The universal implications of non-linear electrodynamics (NED) theory, with the aim of examining the problem of universal evolution, as suggested by the Born-Infeld theory [23–25]. The study has emphasized the significance of NED in the field of cosmology, particularly regarding the time transition that both microscopic and macroscopic regions experience. In the last few years, there has been a significant amount of interest in cosmological models that incorporate NLED, as evidenced by the attention obtained in various studies [26–28]. The study of the NED phenomenon in celestial objects has experienced a notable expansion as a result of noteworthy findings [26,29–31]. The remarkable characteristics of Einstein's gravitational solutions and the NED field are revealed when examining their implications within the framework of the Big Bang cosmological model. The potential significance of NED fields in the cosmos cannot be understated. To have a comprehensive understanding of these solutions, it is essential to recognize the relationship between powerful NED fields. Previous research has investigated BHs characterized by many horizons within the framework of NED fields [32–36]. Recently, the nonlinear BH (RN-BH coupled with the NED parameter ζ) solution has been computed in the framework of the NED field given in Ref. [37]. Also, the first law of thermodynamics Smarr formula, and the physical characteristics of this BH are investigated in [37]. Recently, Ali et.al [38] discussed the quantum thermodynamical properties of RN-AdS BH coupled with a nonlinear electrodynamics field. Furthermore, Sucu and Ovgun [39] investigated the effect of such BH on deflection angle.

With the above motivations, this paper aims to investigate the properties of the circular geodesic and accretion disc surrounding RN-BH coupled with the NED parameter ζ. To be conservative, we restrict our analysis to the polar coordinate system and the equatorial plane and circular orbits and calculate in detail the effects of the NED parameter ζ on r_{ph}, r_{mb}, and r_{isco}. Moreover, the critical accretion is calculated using certain dynamic isothermal fluid parameters. The paper will be completed in the following manner. In Sect. 2, we present a brief review of the RN-BH space-time coupled with the NED parameter ζ. Section 3 is devoted to discussions on the general formulation for particle movement in the given subsections such as flux radiant energy, circular motion, oscillations, and stable circular orbits. In Sect. 4 and its subsections, we determine the generic formulas for numerous dynamical parameters, critical flow speed, accretion for an isothermal fluid, and accretion rate. In Sect. 5, we examined the solution of the RN-BH coupled with the NED parameter ζ and a circular geodesic in the equatorial plane. In Sect. 6 we discuss the summary of this article.

2 Review of black hole spacetime in the NED model

In this section, we present the review of BH solution for the sake of complete understanding of solution, which has been originally formulated by Mazharimousavi [37]. For the charmonium potential given in [37], Guendelman [40,41], the authors have proposed the NED model for the Cornell potential as

$$\mathcal{L} = -\mathcal{F} - g\sqrt{-\mathcal{F}}, \tag{1}$$

here $\mathcal{F} = \frac{1}{4}F_{\mu\nu}F^{\mu\nu}$ is the Maxwell invariant, $\mathcal{L}$ and g refer to the Lagrangian of NED and coupling constant, respectively. For the point charge located at the origin, we use the following differential form [37]

$$\mathbf{F} = E(r)dt \wedge dr, \tag{2}$$

where $E(r)$ represents the radial electric field in the flat spacetime that is expressed by the line element ($c = 1$) that follows

$$ds^2 = dt^2 - dr^2 - r^2(d\theta^2 + \sin^2\theta d\phi^2), \tag{3}$$

The field tensor Eq. (2), fulfils the Bianchi identity, which states that $dF = 0$. Nevertheless, Maxwell's nonlinear equations are represented by

$$d\left(\tilde{\mathbf{F}}\frac{\partial\mathcal{F}}{\partial\mathcal{L}}\right) = 0, \tag{4}$$

while

$$\tilde{\mathbf{F}} = E(r)r^2 \sin(\theta) d\theta \wedge d\phi, \tag{5}$$

represents the Hodge-dual of $\tilde{\mathbf{F}}$. The explicit result of Maxwell's equation is

$$E(r)r^2 \frac{\partial \mathcal{F}}{\partial \mathcal{L}} = C, \tag{6}$$

where constant of integration represented by C. By using $\mathcal{F} = \frac{-1}{2} E^2(r)$ and Eq. (4), one can get

$$E(r) = \frac{q}{r^2} + \frac{g}{\sqrt{2}}, \tag{7}$$

By setting $C = -q$ to obtain the correct Maxwell's linear theory via limit $g \to 0$. The electric potential for the radial electric field Eq. (7) is determined as follows [37]

$$U(r) = \frac{q}{r} - \frac{g}{\sqrt{2}} r, \tag{8}$$

The NED model (5) accurately predicts the charmonium interaction potential energy with suitable parameter adjustments. Similar to Guendelman's approach, one can analyze the NED model for the interaction potentials [37]

$$V_c(r) = -\frac{\alpha_s}{r} + \frac{\alpha_s}{\alpha^2} r, \tag{9}$$

and

$$V_h(r) = -\frac{\alpha}{r} + \frac{\ln(r)}{\alpha}, \tag{10}$$

where α_s, and α represent the charmonium fine structure constant and dimensional parameter, respectively. For the case of NED the coulomb with logarithmic correction interaction one can follow the confinement potential Eq. (10), and present the electric potential [37]

$$U(r) = \frac{q}{r} - g \ln\left(\frac{r}{r_0}\right), \tag{11}$$

wher q and g assumed to be positive. As a result, the radial electric field is produced [37]

$$E(r) = \frac{q}{r^2} + \frac{g}{r}, \tag{12}$$

Further, one can use Maxwell's equation into consideration with an unknown NED Lagrangian Eq. (6), and derive the differential equation that $\mathcal{L}$ must satisfy.

$$\frac{d\mathcal{L}}{dr} = -\frac{q}{r^4}\left(\frac{2q}{r} + g\right), \tag{13}$$

setting $C = -q$ for the same reason as in Eq. (7). The latter equation provides the following result for $\mathcal{L}(r)$

$$\mathcal{L} = \frac{q^2}{r^4} + \frac{qf}{3r^3} + \mathcal{L}_0, \tag{14}$$

here $\mathcal{L}_0$ indicates the integration constant. From Eq. (12), obtained

$$\mathcal{F} = -\frac{1}{2}\left(\frac{q}{r^2} + \frac{g}{r}\right)^2, \tag{15}$$

by setting $\mathcal{L}_0 = 0, g = \zeta\sqrt{q}$ and eliminating r from Eq. (15), then putting into Eq. (14), obtained the following expression [37]

$$\mathcal{L} = -\mathcal{F}\frac{16(3\sqrt{-2\mathcal{F}} + \zeta(\zeta + \sqrt{\zeta^2 + 4\sqrt{-2\mathcal{F}}}))\sqrt{-2\mathcal{F}}}{3(\zeta + \sqrt{\zeta^2 + 4\sqrt{-2\mathcal{F}}})^4} \tag{16}$$

By using $g = \zeta\sqrt{q}$ in Eqs. (12) and (11), the electric field and electric potential attain in the following form

$$E(r) = \frac{q}{r^2} + \frac{g}{r}, \tag{17}$$

and

$$U(r) = \frac{q}{r} - g \ln\left(\frac{r}{r_0}\right), \tag{18}$$

respectively. The action of the NED model is given by [37]

$$S = \int d^4x\sqrt{-g}\left(\frac{R}{16\pi G} + \mathcal{L}\right), \tag{19}$$

where G is the gravitational constant, R indicates the Ricci scalar of the spacetime and $\mathcal{L}$ is given in Eq. (16), being the Maxwell invariant and ζ the coupling constant. For later convenience, hereafter we set $G = 1$. To obtain the spherical symmetric BH solution from Eq. (19), one can start with the following metric ansatz,

$$ds^2 = f(r)dt^2 - \frac{dr^2}{f(r)} - r^2 d\Omega^2, \tag{20}$$

where

$$d\Omega^2 = d\theta^2 + \sin^2\theta d\phi^2, \tag{21}$$

and $f(r)$ is the metric function. The Einstein field equation can be written as

$$G^{\nu}_{\mu} = 8\pi T^{\nu}_{\mu}, \tag{22}$$

where G^{ν}_{μ} is the Einstein tensor and T^{ν}_{μ} is the energy-momentum tensor of the nonlinear electromagnetic field

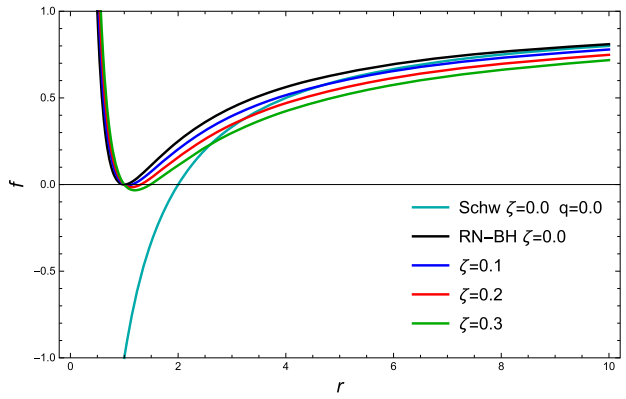

Fig. 1 The plot between lapse function $f(r)$ and r for various values of ζ

which is of the form [37]

$$T_{\mu}^{\nu} = \frac{1}{4\pi}(\mathcal{L}\delta_{\mu}^{\nu} - \mathcal{L}_{\mathcal{F}} F_{\mu\gamma} F^{\nu\gamma}), \tag{23}$$

where $\mathcal{L}_{\mathcal{F}} = \frac{\partial \mathcal{L}}{\partial \mathcal{F}}$. The four components of Einstein's field equations are consistent and practically reduce to

$$G_0^0 = 8\pi T_0^0 = 2\mathcal{L} - 4\frac{\partial \mathcal{L}}{\partial \mathcal{F}}\mathcal{F} \tag{24}$$

From Eq. (24), we have

$$\frac{rf'(r) + f(r) - 1}{r^2} = -\frac{q^2}{r^4} - \frac{2\zeta q^{3/2}}{r^3} - \frac{\zeta^2 q}{r^2} + \frac{\zeta^4}{6} + \frac{\zeta\left(4q^{3/2} + 6\zeta q r - \zeta^3 r^3\right)}{6r^3}, \tag{25}$$

The above expression simplifies to

$$\frac{rf'(r) + f(r) - 1}{r^2} = -\frac{q^2}{r^4} - \frac{4\zeta q\sqrt{q}}{3r^3}, \tag{26}$$

By solving the above equation one can obtain the following metric

$$f(r) = 1 - \frac{2M}{r} + \frac{q^2}{r^2} - \frac{4q\sqrt{q}\zeta}{3r}\ln(r). \tag{27}$$

where M is the mass of BH, q is electric charge and ζ is the NED parameter. The nature of the spacetime, whether it represents a singular BH or a particle with a naked singularity, depends on the values of the NED parameter as well M (mass) and q (charge) of the BH. We determine the BH horizons by considering the lapse function $f(r) = 0$. The horizons structure of considered BH represented in Fig. 1. The horizon of Schwarzschild BH is indicated by a cyan curve, RN-BH is represented by a black curve and remanning curves represent the horizon radius of considered BH.

3 General formulation for the geodesic motion of test particles

This section establishes the general formulation for the geodesic motion of the massive test particles by examining the RN-BH coupled NED parameter ζ, which follows timelike geodesics. We assume $\xi_t = \partial_t$ and $\xi_\phi = \partial_\phi$ are killing vectors associated with fundamental constants, indicated as E and L (conserved energy and angular momentum) associated with the specified trajectory

$$E = -g_{\mu\nu}\xi_t^{\mu} u^{\nu} \equiv -u_t, \tag{28}$$

and

$$L = g_{\mu\nu}\xi_{\phi}^{\mu} u^{\nu} \equiv u_{\phi}, \tag{29}$$

where $u^{\mu} = \frac{dx^{\mu}}{d\tau} = (u^t, u^r, u^{\theta}, u^{\phi})$ is the four-velocity vector with τ being the affine parameter of the timelike geodesics. For timelike geodesics, the four-velocity vector u^{μ} fulfills the normalization condition $u^{\mu}u_{\mu} = 1$ and then one obtains

$$[g_{rr}(u^r)^2 + g_{\theta\theta}(u^{\theta})^2] = [1 - g^{tt}(u_t)^2 - g^{\phi\phi}(u_{\phi})^2]. \tag{30}$$

From Eqs. (28), (29) and (30), in the equatorial plane (i.e. $\theta = \frac{\pi}{2}$), we have

$$u^t = -\frac{E}{f(r)}, \tag{31}$$

$$u^{\theta} = 0, \tag{32}$$

$$u^{\phi} = -\frac{L}{r^2}, \tag{33}$$

and

$$u^r = \sqrt{-f(r)\left(1 - \frac{E^2}{f(r)} + \frac{L^2}{r^2}\right)}. \tag{34}$$

Then Eq. (34) gives

$$(u^r)^2 + V_{eff} = E^2, \tag{35}$$

where

$$V_{eff} = f(r)\left[1 + \frac{L^2}{r^2}\right], \tag{36}$$

is the effective potential. From the above result, it is obvious that the effective potential relies on the radial distribution, angular momentum, and space-time parameter $f(r)$. The effective potential is incredibly helpful in the geodesic motion of the particles due to its ability to identify the position of ISCO by analyzing the local extrema of the effective potential.

3.1 Circular motion of test particles

Let us first consider the circular motion of the massive particles in the equatorial plane ($\theta = \pi/2$). For circular motion, one has the conditions

$$u^r = \frac{dr}{d\tau} = 0 \quad \text{and} \quad \dot{u}^r = \frac{d^2r}{d\tau^2} = 0. \tag{37}$$

With these two conditions and by using Eq. (35), one has

$$V_{eff} = E^2 \quad \text{and} \quad \frac{d}{dr}V_{eff} = 0. \tag{38}$$

Then one can obtain the angular velocity Ω_ϕ, specific energy E, and the specific angular momentum L associated with the test particle that are provided respectively by

$$\Omega_\phi^2 = \frac{1}{2r}f'(r), \tag{39}$$

$$E^2 = \frac{2f^2(r)}{2f(r) - rf'(r)}, \tag{40}$$

and

$$L^2 = \frac{r^3 f'(r)}{2f(r) - rf'(r)}. \tag{41}$$

Frome Eqs. (40) and (41), E and L should be real if

$$2f(r) - rf'(r) > 0. \tag{42}$$

From the above expression, the specific area of the circular orbit can be investigated. So, the inequality (42), is essential for the existence of circular orbits. For bound orbits, one requires $E^2 < 1$ while the marginally bound orbit corresponds to $E^2 = 1$. Thus the marginally bound orbit satisfies

$$2[f(r) - 1]f(r) + rf'(r) = 0. \tag{43}$$

This equation determines the radius of the marginally bound orbit. On the other hand, it is easy to see that Eqs. (40) and (41) diverge if

$$-rf'(r) + 2f(r) = 0. \tag{44}$$

With this equation, one can determine the photon sphere radius which is essential for the investigation of gravitational lensing.

3.2 Radiant energy flux and circular orbits

The presence of stable circular orbits is dependent upon the local minima of the effective potential, which is attained when $\frac{d^2V_{eff}}{dr^2} > 0$. From Eq. (36), we have

$$\frac{d^2V_{eff}}{dr^2} = \left(1 + \frac{L^2}{r^2}\right)f''(r) - \frac{4L^2}{r^3}f'(r) + \frac{6L^2}{r^4}f(r). \tag{45}$$

By employing the requirements $V_{eff} = 0$, $\frac{dV_{eff}}{dr} = 0$, and $\frac{d^2V_{eff}}{dr^2} = 0$, one is able to calculate the radius of ISCO, i.e.,r_{isco}. Furthermore, the process of accretion is possible in $r < r_{isco}$. When particles fall from a state of rest to an infinite distance, accreting onto compact objects, they emit gravitational energy, which is converted into radiation. In [42], the expression for the energy flux radiating across the accretion disc is formulated on the basis of the angular velocity Ω_ϕ, the specific energy E, and the specific angular momentum L as

$$K = -\frac{\dot{M}\Omega_{\phi,r}}{4\pi\sqrt{-g}(E - L\Omega_\phi)^2}\int_{r_{isco}}^{r}(E - L\Omega_\phi)L_{,r}\,dr, \tag{46}$$

where radiant flux is represented by K, mass accretion rate is $\dot{M}$, $\Omega_{\phi,r} \equiv \frac{d\Omega_\phi}{dr}$ and g is the determinant of the metric tensor $g_{\mu\nu}$. g is given by

$$g = \det(g_{\mu\nu}) = -r^4\sin^2\theta, \tag{47}$$

In order to properly analyze our findings within the equatorial plane, we establish the relationship $\sin\theta = \sin\frac{\pi}{2} = 1$. By utilizing Eqs. (39–41) and the of values g, $\Omega_{\phi,r} \equiv \frac{d\Omega_\phi}{dr}$, $L_{,r} = \frac{dL}{dr}$ in Eq. (46), we obtain

$$K(r) = \frac{-\dot{M}}{4\pi r^4}\sqrt{\frac{r}{2f'(r)}} \times \frac{[rf'(r) - 2f(r)][rf''(r) - f'(r)]}{[2f(r) + rf'(r)]^2}\int_{r_{isco}}^{r}F(r)dr, \tag{48}$$

where the function $F(r)$ is given by

$$F(r) = \sqrt{\frac{r}{2f'(r)}}\Big[rf'(r) + 2f(r)\Big] \times \frac{rf(r)f''(r) - 2rf'^2(r) + 3f(r)f'(r)}{[2f(r) - rf'(r)]^2}. \tag{49}$$

We assume that the accretion disc is in a state of thermal equilibrium, thus according to the Stefan-Boltzmann law, one has $K(r) = \sigma T^4(r)$ with σ being the Stefan-Boltzmann constant, which is the relation between energy flux and temperature. Consequently, the radiation produced from the accretion disc is presumed to possess characteristics similar to those of black body radiation. By considering the thermal black body radiation, it is simple to determine the temperature distribution of the accretion disc by utilizing the given equation, from which one can figure out disc luminosity $L(\nu)$ where ν is the frequency of the radiated photons. The disc luminosity is determined by [43]

$$L(\nu) = 4\pi d^2 I(\nu) = \frac{8\cos\gamma}{\pi}\int_{r_{isco}}^{r}\int_0^{2\pi}\frac{\nu_e^3 r}{\exp(\frac{\nu_e}{T}) - 1}d\phi dr. \tag{50}$$

where γ is the inclination angle of the accretion disc and $I(\nu)$ is the thermal energy flux. The emitted frequency is given by $\nu_e = \nu(1+z)$ where ν is the observed frequency of the radiation and z represents the redshift factor. By neglecting the bending of light, the redshift factor z is obtained [20].

$$z = \frac{1 + \Omega_\phi r \sin\phi \sin\gamma}{\sqrt{-g_{tt} - \Omega_\phi^2 g_{\phi\phi}}} - 1. \tag{51}$$

From Eq. (50), it is clear that the luminosity $L(\nu)$ depends on the disc's temperature T. The emission at every radius r is influenced by temperature T through the exponential term in the denominator of the integrand. The expression $exp(\frac{\nu_e}{T}) - 1$ in the denominator implies that as temperature T increases, the factor becomes smaller, which leads to the increase in luminosity $L(\nu)$. So, higher temperatures at higher frequencies will provide a higher luminosity $L(\nu)$. Moreover, accreting flow efficiency is another component of the mass accretion process. The maximum efficiency η^* can be obtained by

$$\eta^* = 1 - E_{isco}. \tag{52}$$

Here, E_{isco} is the energy of the particles at ISCO. This proceeding relation holds when all emitted photons have the ability to escape infinity. When a fluid element experiences a perturbation, the resulting particles move, which corresponds to a circular orbit within the plane $\theta = \frac{\pi}{2}$.

3.3 Oscillations

In accretion processes, numerous types of oscillatory motion are seen as a result of restoring forces. The oscillatory motion in both the horizontal and vertical directions arises from the influence of restoring forces acting upon perturbations within the accretion discs. In an accretion disc, the number of restoring forces arises from the rotational motion of the disc in the presence of a vertical gravitational field.

When a fluid element moves radially, it returns to its state of equilibrium through the rotational motion of the fluid by virtue of the presence of a restoring force. It is worth noting that the gravitational force within accretion discs serves as a counterbalance to the centrifugal force due to central objects. The fluid element is dragged outside or inside and returned towards the original radius utilizing Ω_r epicyclic frequency, depending on whether the latter exceeds the former or vice versa. When the fluid element encounters a vertical perturbation within the plane $\frac{\pi}{2}$, the field of gravitation pinches the elements that are perturbed, causing it to return to its original equilibrium state. The element of fluid exhibits harmonic oscillations within the equatorial plane due to the presence of a restoring force, characterized by a vertical epicyclic frequency Ω_θ. Three different types of motion, harmonic vertical motion with a vertical frequency, circular motion with an orbital frequency, and radial motion with a radial frequency, are responsible for the behavior of particles within the accretion disc. Consequently, within the equatorial plane, we can examine the redial motion and vertical motion in the vicinity of circular orbits.

Now, let us investigate the radial and vertical motions that are represented by $\frac{1}{2}\left(\frac{dr}{dt}\right)^2 = V_{eff}^{(r)}$ and $\frac{1}{2}(\frac{d\theta}{dt})^2 = V_{eff}^{(\theta)}$, exhibited by the particles under consideration, where using Eq. (30) for explain the radial and vertical motions we consider $u^\theta = 0$, $u^r = 0$, respectively. Considering $u^r = \frac{dr}{d\tau} = \frac{dr}{dt}u^t$ and $u^\theta = \frac{d\theta}{d\tau} = \frac{d\theta}{dt}u^t$, we can deduce the following equations,

$$\frac{1}{2}\left(\frac{dr}{dt}\right)^2 = -\frac{1}{2}\frac{f^3(r)}{E^2}\left[1 - \frac{E^2}{f(r)} + \frac{L^2}{r^2\sin^2(\theta)}\right] = V_{eff}^{(r)} \tag{53}$$

and

$$\frac{1}{2}\left(\frac{d\theta}{dt}\right)^2 = -\frac{1}{2}\frac{f^2(r)}{E^2 r^2}\left[1 - \frac{E^2}{f(r)} + \frac{L^2}{r^2\sin^2\theta}\right] = V_{eff}^{(\theta)}. \tag{54}$$

In the equatorial plane, we shall investigate the vertical and radial epicyclic frequencies in the vicinity of circular orbits by considering small perturbations denoted as δr and $\delta\theta$. Differentiating Eq. (53) and Eq. (55) with respect to time t, one obtains

$$\frac{d^2r}{dt^2} = \frac{dV_{eff}^{(r)}}{dr}. \tag{55}$$

For a particle having a perturbation in its original radius at $r = r_0$, characterized by a deviation $\delta r = r - r_0$, the resulting equation can be expressed as follows

$$\frac{d^2}{dt^2}(\delta r) = \frac{d^2V_{eff}^{(r)}}{dr^2}(\delta r) \Rightarrow (\delta\ddot{r}) + \Omega_r^2(\delta r) = 0, \tag{56}$$

where $\Omega_r^2 \equiv -\frac{d^2}{dr^2}V_{eff}^{(r)}$ and dots denotes derivatives with respect to t. Through an analogous methodology, when considering a perturbation in the vertical direction $\delta\theta = \theta - \theta_0$, we arrive at the following result

$$\frac{d^2(\delta\theta)}{dt^2} = \frac{d^2V_{eff}^{(\theta)}}{dr^2}(\delta\theta) \Rightarrow (\delta\ddot{\theta}) + \Omega_\theta^2(\delta\theta) = 0, \tag{57}$$

where $\Omega_\theta^2 \equiv -\frac{d^2}{d\theta^2}V_{eff}^{(\theta)}$. In the Equatorial plane, Eqs. (53) and (55) lead to

$$\begin{aligned}\Omega_r^2 = \frac{1}{2E^2r^4}\Big\{&\left[(r^2+L^2)3f(r) - 2E^2r^2\right]r^2f(r)f''(r)\\ &+2r^2\left[(r^2+L^2)3f(r) - E^2r^2\right]f'^2(r)\\ &-6L^2f^2(r)\left[2rf'(r) - f(r)\right]\Big\},\end{aligned} \tag{58}$$

and

$$\Omega_\theta^2 = \frac{f^2(r)L^2}{E^2 r^4}. \tag{59}$$

The prime notation in Eq. (58) denotes differentiation with respect to the radial coordinate r. The subsequent section presents a comprehensive investigation of the fundamental dynamical equations governing RN-BH coupled with NED.

4 Basic dynamical equations

In this section, we performed an analysis of the fundamental formalism for the accretion process around RN-BH coupled with NED. For this purpose, we follow the fundamental formalism that was established by Babichev et al. [44,45]. Let us start by considering an ideal fluid that is characterized by its energy-momentum tensor

$$T^{\mu\nu} = (\rho + p)u^\nu u^\mu + g^{\mu\nu} p. \tag{60}$$

The quantities denoted as p and ρ correspond to the pressure and energy density of the fluid, respectively. In the equatorial plane, the four-velocity u^μ can be described as follows

$$u^\mu = \frac{dx^\mu}{d\tau} = (u^t, u^r, 0, 0), \tag{61}$$

where τ is the proper time. By combining the above equation with the normalization condition ($u^\mu u_\mu = 1$), we obtain

$$u^t = \frac{\sqrt{f(r) + (u^r)^2}}{f(r)}. \tag{62}$$

The requirement $u^t > 0$ indicates flow is forward, whereas for accretion (flow is inward), the assumption $u^r < 0$ holds. In order to analyze the accretion process, it is necessary to calculate the conservation equation of energy-momentum and conservation equation of particle-number. The conservation of energy-momentum tensor reads $T^{\mu\nu}_{;\mu} = 0$, which leads to

$$T^{\mu\nu}_{;\mu} = \frac{1}{\sqrt{-g}}(\sqrt{-g}T^{\mu\nu})_{,\mu} + \Gamma^\nu_{\alpha\mu}T^{\alpha\mu} = 0, \tag{63}$$

where $\sqrt{-g} = r^2 \sin\theta$, Γ is Christoffel symbol's of 2nd kind and $(;)$ is the covariant derivative associated with the metric $g_{\mu\nu}$. By utilizing the BH metric, Eq. (63) can be transformed into the form of

$$T^{rt}_{,r} + \frac{1}{\sqrt{-g}}T^{rt}(\sqrt{-g})_{,r} + 2\Gamma^t_{tr}T^{rt} = 0. \tag{64}$$

By solving Eq. (64), one has

$$\frac{d}{dr}[(\rho + p)u^r r^2\sqrt{f(r) + (u^r)^2}] = 0. \tag{65}$$

By performing the integration on the above equation, we are able to derive the resulting expression

$$(\rho + p)u^r r^2\sqrt{f(r) + (u^r)^2} = C_0. \tag{66}$$

In Eq. (66), C_0 represents the integration constant. Using the principle of conservation coupled with the four-velocity, as expressed by the equation $u_\mu T^{\mu\nu}_{;\nu} = 0$, we attain

$$\begin{aligned}&(\rho + p)u^\mu_{;\nu}u_\mu u^\nu + (\rho + p)_{,\nu}u_\mu u^\mu u^\nu \\ &+(\rho + p)u_\mu u^\mu u^\nu_{;\nu} + p_{,\nu}g^{\mu\nu}u_\mu + pu_\mu g^{\mu\nu}_{;\nu} = 0.\end{aligned} \tag{67}$$

Since $g^{\mu\nu}_{;\nu} = 0$ and utilizing $u^\mu u_\mu = 1$, one gets

$$(p + \rho)u^\nu_{;\nu} + u^\nu \rho_{,\nu} = 0, \tag{68}$$

and since $A^b_{;a} = \partial_a A^b + \Gamma^b_{ac}A^c$, we acquire

$$\begin{aligned}&u^r\rho_{,r} + [\Gamma^t_{tc}u^c + u^r_{,r} + \Gamma^r_{rc}u^c + \Gamma^\theta_{\theta c}u^c + \Gamma^\phi_{\phi c}u^c] \\ &\times(\rho + p) = 0.\end{aligned} \tag{69}$$

From Eq. (69), we attain

$$\frac{\rho'}{(\rho + p)} + \frac{u'}{u} + \frac{2}{r} = 0, \tag{70}$$

and solving it yields

$$r^2 u^r \exp\left(\int \frac{d\rho}{p + \rho}\right) = -C_1, \tag{71}$$

where C_1 is the integration constant. Assuming $u^r < 0$, it follows that the above expression also has a negative sign and we calculate

$$(p + \rho)\sqrt{(u^r)^2 + f(r)}\exp\left(-\int \frac{d\rho}{p + \rho}\right) = C_2. \tag{72}$$

The constant of integration, indicated as C_2 and the flux mass equation is

$$(\rho u^\mu)_{;\mu} \equiv \frac{1}{\sqrt{-g}}(\sqrt{-g}\rho u^\mu)_{,\mu} = 0. \tag{73}$$

Then utilizing Eq. (73), we get

$$\frac{1}{\sqrt{-g}}(\sqrt{-g}\rho u^r)_{,r} + \frac{1}{\sqrt{-g}}(\sqrt{-g}\rho u^\theta)_{,\theta} = 0. \tag{74}$$

Note that the term $\frac{1}{\sqrt{-g}}(\sqrt{-g}\rho u^\theta)_{,\theta}$ in Eq. (74) can be omitted since we only focus on the equatorial plane. Therefore, the expression $\sqrt{-g}\rho u^r$ is considered to be constant, i.e.,

$$\rho u^r r^2 = C_3, \tag{75}$$

where C_3 represents the integration constant.

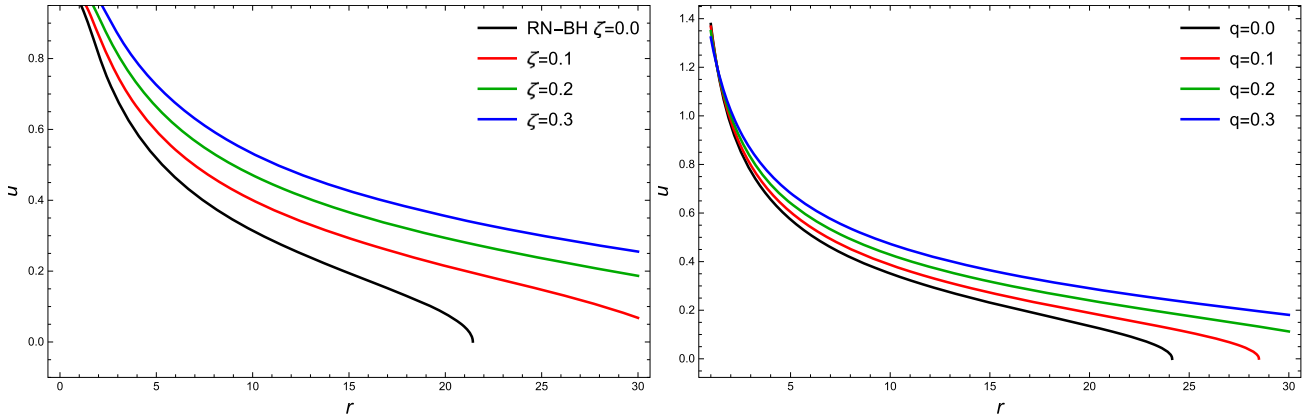

Fig. 2 The behaviors of u as a function of dimensionless radius r for $M = 1$, different values of electric charge q and the NED paramater ζ. The left panel corresponds to a fixed $q = 1$ various values of ζ and the right panel corresponds to a fixed $\zeta = 1.5$ various values of electric charge q

4.1 Dynamical parameters

Let us examine the accretion of the isothermal fluids characterized by the equation of state $p = k\rho$, where k is the state function. For isothermal fluid $p \propto \rho$ it is necessary that the speed of sound remain constant in the accretion procedure. Moreover, from Eqs. (71), (72) and (75), one can determine

$$\frac{\rho + p}{\rho}\sqrt{f(r) + (u^r)^2} = C_4, \tag{76}$$

where C_4 represents the integration constant. Considering $p = k\rho$ and substitute it into Eq. (76), one has

$$u = \frac{\sqrt{C_4^2 - \frac{(k+1)^2[3(-2Mr+q^2+r^2)-4\zeta q^{3/2} r \ln r]}{3r^2}}}{k+1}. \tag{77}$$

The graphs presented in Fig. 2 illustrate the relationship between radial velocity u and r. When the fluid is farthest from the BH, it has zero radial velocity and moves with subsonic speed before the critical points. At the critical point, the rate of flow matches the speed of sound. As the fluid crosses critical points in the vicinity of the BH, the flow rate increases and enters the supersonic domain due to the strong gravity of the BH. The impact of the coupling parameter ζ on the radial velocity is shown in the left panel, while the effect of electric charge q is represented in the right panel. In the left panel of Fig. 2, we analyze that radial velocity increases with increasing the coupling parameter ζ. In the right panel of Fig. 2, we observe that the radial velocity increases gradually by increasing the electric charge parameter q. As a result, infalling particles accelerate with the speed of sound near the central mass.

Now we can determine the density of fluid from Eq. (75), which is given by

$$\rho = \frac{C_3(k+1)}{r^2\sqrt{C_4^2 - \frac{(k+1)^2(3(-2Mr+q^2+r^2)-4\zeta q^{3/2} r \ln(r))}{3r^2}}}. \tag{78}$$

The behavior of ρ as a function of dimensionless radius r for different values of the electric charge and the NED parameter ζ are presented in Fig. 3. It is observed that the fluid has small density at the outer part of the disc and increases gradually as it moves to the inner part of the disc. Notably, the blue and green curves show the effects of the NED parameter ζ while the black curve indicates the behavior of RN-BH in the left panel of Fig. 3. It can be easily seen that as the value of the NED parameter increases, the density of the fluid decreases. Moreover, in the right panel of Fig. 3, we have observed that fluid density declines by increasing the value of electric charge q.

4.2 Mass evolution

Based on astronomical investigation, it is proposed that the mass of BH gradually varies over time due to various phenomena such as the emission of Hawking radiation and mass accreting around the BH. The mass accretion rate of RN-BH coupled with the NED parameter ζ can be computed as $\dot{M} \equiv \frac{dM}{dt} = -\int T_t^r ds$ in which $ds = \sqrt{-g}d\theta d\phi$ and also $T_t^r = (p+\rho)u_t u^r$. As a consequence, accretion rate $\dot{M}$ is acquired by

$$\dot{M} = -4\pi r^2 u(p+\rho)\sqrt{u^2 + f(r)} \equiv -4\pi C_0. \tag{79}$$

By asssuming $C_0 = -C_1 C_2$ and $C_2 = (p_\infty + \rho_\infty)\sqrt{f(r_\infty)}$, we have

$$\dot{M} = 4\pi C_1(p_\infty + \rho_\infty)\sqrt{f(r_\infty)}M^2. \tag{80}$$

The evolution of time and BH mass can be obtained by considering M_i is the initial mass and utilizing the Eq. (80), we obtained

$$\frac{dM}{M^2} = \mathcal{F}t, \tag{81}$$

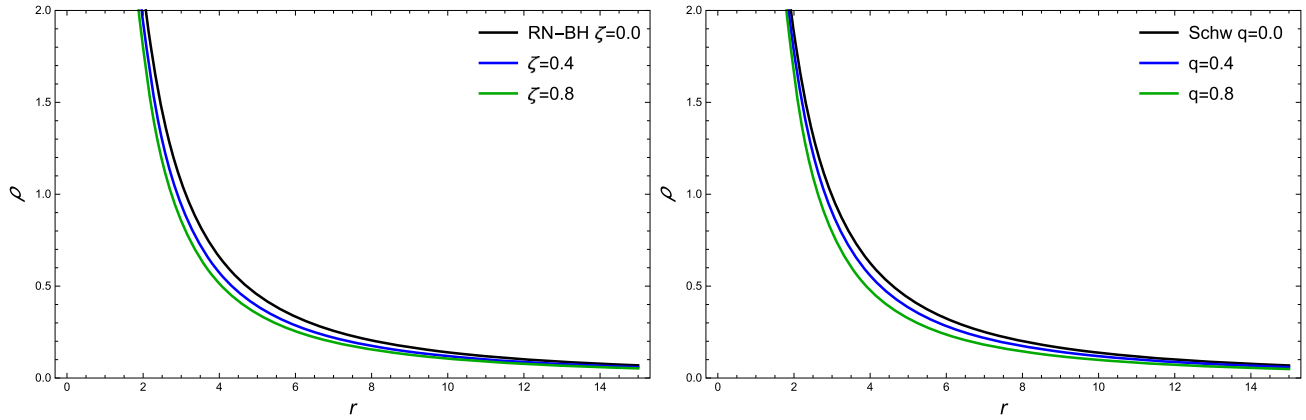

Fig. 3 The behaviors of the fluid density ρ as a function of dimensionless radius r for $M = 1$, different values of electric charge q and the NED parameter ζ. The left panel corresponds to a fixed $q = 1$ various values of ζ and the right panel corresponds to a fixed $\zeta = 1.5$ various values of electric charge q

where $\mathcal{F} \equiv 4\pi C_1(p+\rho)\sqrt{f(r_\infty)}$. From Eq.(81), we have

$$M_t = \frac{M_i}{1-\mathcal{F}M_i t} \equiv \frac{M_i}{1-\frac{t}{t_{cr}}}, \tag{82}$$

the expression for the time accretion t_{cr} is calculated by using the formula $t_{cr} = [4\pi C_1(p+\rho)\sqrt{f(r_\infty)}M_i]^{-1}$. According to Eq. (82), it is evident that at $t = t_{cr}$, the BH mass increases. So, the mass accretion rate of a BH is

$$\dot{M} = 4\pi C_1(p+\rho)M^2. \tag{83}$$

Figure 4 depicts the relationship between the mass accretion rate and the variable r. It is observed that the accretion rate increases in the vicinity of the BH due to its strong gravitational field. The effect of NED parameter ζ and charge q are shown in left and right panel of Fig. 4 respectively. In left plot we note that the accretion rate $\dot{M}$ decreases with increasing the NED parameter ζ while in right plot it can be seen that the mass accretion rate decreases with increasing the electric charge q. This behavior investigated by Rodrigues et al. [46] for a Schwarzschild BH in the framework of anon-minimally coupled scalar filed. They discovered that the accretion of the scalar field can lead to a mass decrease for BHs whose initial masses are less than a critical values, even in the absence of phantom energy and Hawking radiation. Furthermore, the BH with initial masses larger than the critical value increases by accreting a scalar field similar to the minimal coupled scalar case. In [20] Salahshoor and Nozari also studied this behavior for Horndeski/Galileon BH. They found that the BH mass increases with increasing correction factor due to its strong gravitational pull.

4.3 Critical accretion

The flow of fluid is static farthest from the BH, but it starts to move and accelerates inward due to the gravitational field exerted by the BH. When fluid flows inward, it reaches a sonic point where the velocity of the fluid is equivalent to the speed of sound. By utilizing Eqs. (75) and (76), we have

$$\frac{\rho'}{\rho} + \frac{u'}{u} + \frac{2}{r} = 0, \tag{84}$$

and

$$\frac{\rho'}{\rho}\left[\frac{d\ln(p+\rho)}{d\ln\rho} - 1\right] + \frac{uu'}{u^2+f(r)} + \frac{1}{2}\frac{f'(r)}{u^2+f(r)} = 0. \tag{85}$$

From Eq. (85), we attain

$$\frac{d\ln u}{d\ln r} = \frac{D_1}{D_2}, \tag{86}$$

where

$$D_1 = \frac{rf'(r)}{2(u^2+f(r))} - 2V^2, \tag{87}$$

and

$$D_2 = V^2 - \frac{u^2}{u^2+f(r)}. \tag{88}$$

From Eqs. (86)–(88), we attain

$$V^2 = \frac{d\ln(p+\rho)}{d\ln\rho} - 1. \tag{89}$$

We assume smooth flow throughout spacetime. However, if the denominator D_1 vanishes, the numerator D_2 must vanish. Mathematically, This point is known as the critical point of the flow [47]. In (86), for $D_1 = D_2 = 0$ there is $\frac{0}{0}$ form at the critical point we must apply L'Hospital's Rule to calculate the gradient of radial velocity at r_c. The critical point determined by assuming $D_1 = D_2 = 0$ which yields

$$V_c^2 = \frac{rf'(r)}{4f(r)+rf'(r)}, \tag{90}$$

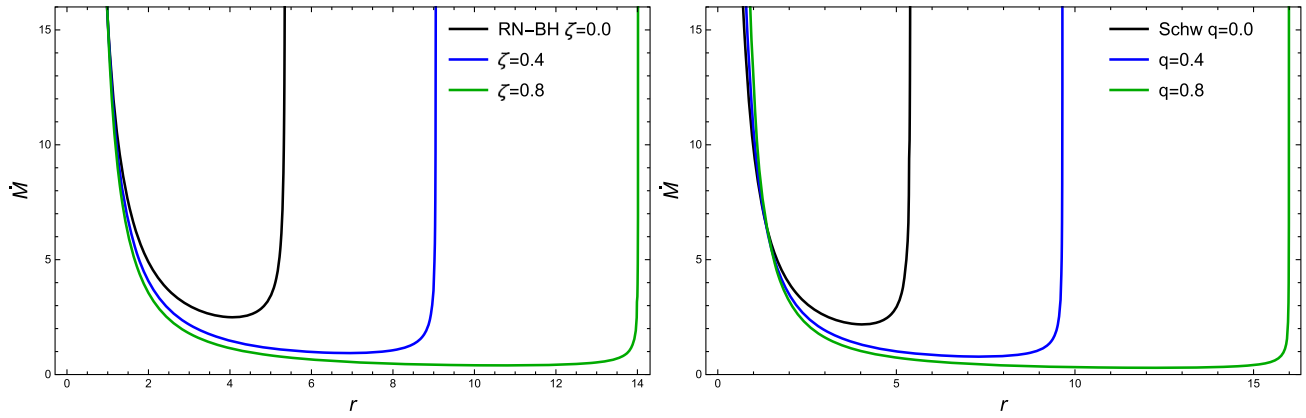

Fig. 4 The mass accretion rate $\dot{M}$ as a function of r for different values of electric charge q and the NED paramater ζ. The left panel corresponds to a fixed $q = 1$ various values of ζ and the right panel corresponds to a fixed $\zeta = 1.5$ various values of electric charge q

and

$$u_c^2 = \frac{1}{4} r f'(r). \tag{91}$$

The index c is referred to as the critical point. Note that the right-hand side of Eq. (89) is always positive. We compute the critical radius range by using the subsequent expression

$$4f(r) + rf'(r) > 0. \tag{92}$$

By utilizing Eq. (77), we acquire

$$c_s^2 = C_4 \sqrt{[u^2 + f(r)]^{-1}} - 1. \tag{93}$$

The relation that represents the speed of sound is given by $c_s^2 = \frac{dp}{d\rho}$.

5 Circular equatorial geodesics

The effective potential is necessary to examine circular geodesics in the plane $\theta = \frac{\pi}{2}$, which is obtained from Eq. (36) as

$$V_{eff} = \left(1 - \frac{2M}{r} + \frac{q^2}{r^2} - \frac{4\zeta q\sqrt{q}\ln r}{3r}\right)\left(1 + \frac{L^2}{r^2}\right). \tag{94}$$

The graphs presented in Fig. 5 illustrate the behaviors of the effective potential as a function of the radial coordinate r for different values of the specific angular momentum L, electric charge q, and the NED parameter ζ. In Fig. 5a, one can observe the first extrema exist at $L = 5$ and no other extrema arise for $L < 5$. Additionally, the effective potential increases when angular momentum L rises. The black dot within Fig. 5a gives the precise location of the ISCO, situated at $r = 4.26944$. Furthermore, the effective potential V_{eff} reveals two extrema for higher values of L. The stable and unstable circular orbits lie at the minimum and maximum of V_{eff}, respectively. From Fig. 5b, it is clear that as the value of BH parameter ζ rises, the effective potential decreases. In addition, from Fig. 5c, we observe that how the BH charge q affects the effective potential V_{eff} along r. In Fig. 5c, we can see V_{eff} declines as the value of charge q increases. We are currently interested in calculating ISCO for RN-BH coupled with NED because it forms the inner edges of the accretion disc, so the role of ISCO is significant. Unfortunately, we are unable to determine the ISCO analytically. Therefore, we will have to turn to numerical approaches by utilizing the general formula for ISCO provided in reference [48]. Whenever $\zeta = 0.1$, $M = 1$, and the charge $q = 1$, the ISCO of BH is $r_{isco} = 4.26944$. More detail regarding this can be found in Table 1.

In order to thoroughly investigate the accretion process, the ISCO is significant. It is also mandatory to conduct an analysis of other radii to obtain a comprehensive understanding. As previously mentioned, a circular orbit is present when the value of $r > r_{ph}$. The particle's motion will demonstrate instability for small perturbations when the radial distance lies within the range of $r_{ph} < r < r_{isco}$. This relationship suggests that particles either escape to infinity or are dragged into the BH. If $r > r_{isco}$., the particle proceeds to move in stable circular orbits. Also, the photon sphere r_{ph}, circular orbit r_{isco} and marginally bound orbit r_{mb} are given in Table 1

In the plane $\theta = \frac{\pi}{2}$, one can derive the formulas for the following quantities

$$E^2 = \frac{1}{3r^2}\frac{\left[3\left(r(r-2M)+q^2\right) - 4\zeta q^{3/2} r\ln r\right]^2}{3r(r-3M) + 2\zeta q^{3/2} r - 6\zeta q^{3/2} r\ln r + 6q^2}, \tag{95}$$

$$L^2 = \frac{3r^2\left(3Mr - 2\zeta q^{3/2} r + 2\zeta q^{3/2} r\ln r - 3q^2\right)}{3r(r-3M) + 2\zeta q^{3/2} r - 6\zeta q^{3/2} r\ln r + 6q^2}, \tag{96}$$

and

$$\Omega_\phi^2 = \frac{3Mr - 2\zeta q^{3/2} r + 2\zeta q^{3/2} r\ln r - 3q^2}{3r^4}. \tag{97}$$

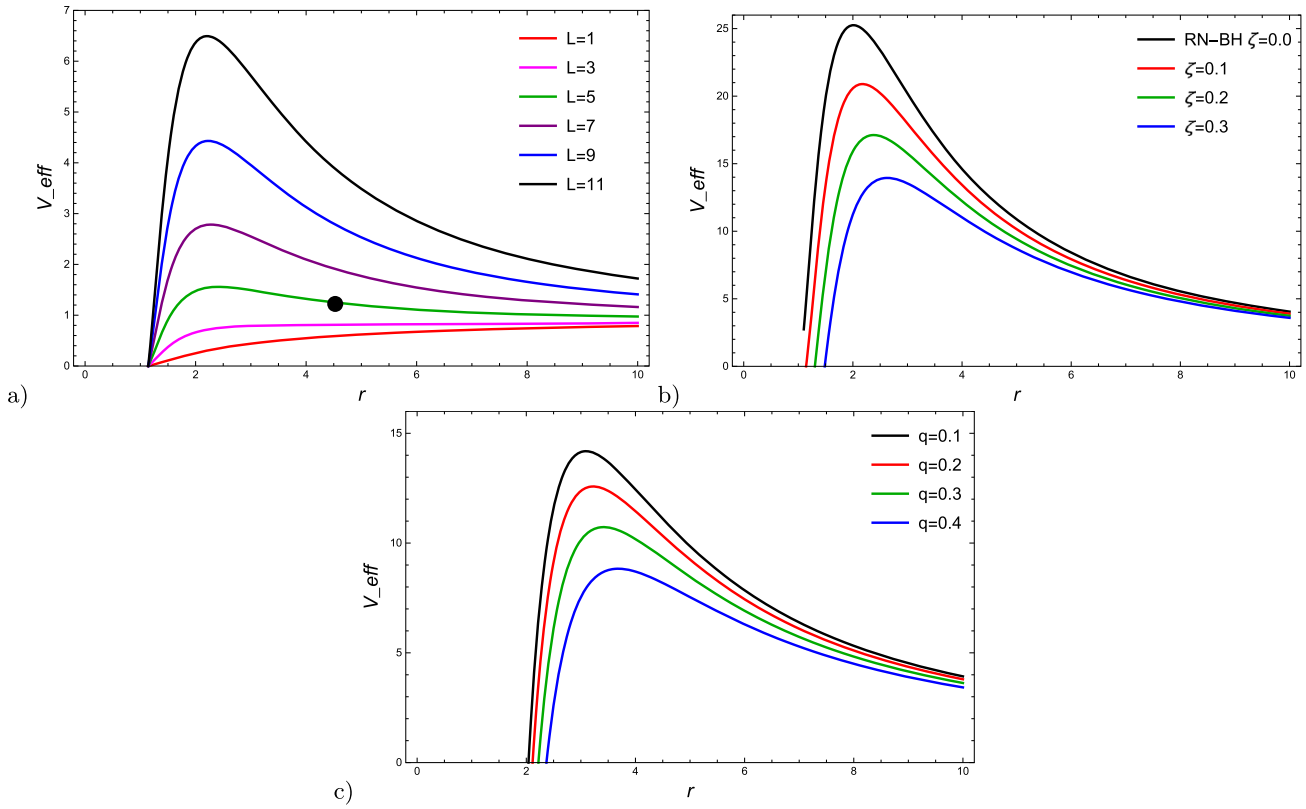

Fig. 5 The illustration of V_{eff} is a function of dimensionless radius r. **a** For $\zeta = -1.5$, $q = 1$, and altered values of L; **b** for $q = 1$, $L = 10$ and various values of ζ; **c** for $\zeta = -1.5$, $L = 10$ and distinct values of q

Figure 6 depicts the specific energy and specific angular momentum profile along r. Also, the effects of BH parameters ζ and charge q have been investigated in the given plots. Presently, our focus to analyze the following quantities E_{isco}, L_{isco}, Ω_{isco}, and l_{isco} in ISCO. However, it is worth noting that an analytical identification of all these quantities is not possible. Therefore, the numerical calculation is outlined in the provided table.

5.1 Radiant energy flux

We begin to investigate the flux radiation emanating from the outermost layer of the disc in the plane $\theta = \frac{\pi}{2}$ by the utilization of the corresponding quantities E, L, and Ω_ϕ. The flux radiant energy associated with the accretion disc can be investigated through Eqs. (48) and (49), given as

$$K(r) = -\Bigg\{\sqrt{3}\dot{M}\sqrt{\frac{r^4}{3Mr - 2\zeta q^{3/2}r + 2\zeta q^{3/2}r\ln r - 3q^2}} \times\Big(9Mr - 8\zeta q^{3/2}r + 6\zeta q^{3/2}r\ln r - 12q^2\Big) \times\Big[3r(-2Mr - M + r^2) + 2\zeta q^{3/2}r - 2\zeta q^{3/2}r(2r+1)\ln r + 3q^2(r+1)\Big]\Bigg\}$$
$$\times\Big[8\pi r^5(3r(-2Mr + M + r^2) - 2\zeta q^{3/2}r + 2\zeta q^{3/2}r(1-2r)\ln r + 3q^2(r-1))^2\Big]^{-1}\int_{r_{isco}}^{r} F(r)dr, \quad (98)$$

where

$$F(r) = \Bigg\{\sqrt{\frac{r^4}{9Mr - 6\zeta q^{3/2}r + 6\zeta q^{3/2}r\ln r - 9q^2}} \times\Big[3r(-2Mr + M + r^2) - 2\zeta q^{3/2}r + 2\zeta q^{3/2}r(1-2r)\ln r + 3q^2(r-1)\Big] \times\Big[2\zeta q^{3/2}r\ln(r)(3r(r^2 - 4M(r+2)) + 16\zeta q^{3/2}r - 4\zeta q^{3/2}r(r+2)\ln r + 3q^2(r+8)) - 48\zeta q^{3/2}r(q^2 - Mr) + 9(Mq^2r(r+8) + Mr^2(r^2 - 2M(r+2)) - 4q^4) - 16\zeta^2 q^3 r^2\Big]\Bigg\} \quad (99)$$
$$\times\Big(2r^3(3r(-2Mr - M + r^2) + 2\zeta q^{3/2}r - 2\zeta q^{3/2}r(2r+1)\ln r + 3q^2(r+1))^2\Big)^{-1}. \quad (100)$$

In order to analyze the radiation flux behavior of the accretion disc surrounding BH for numerous values of the coupling parameter ζ, as depicted in Fig. 7, it is observed that as

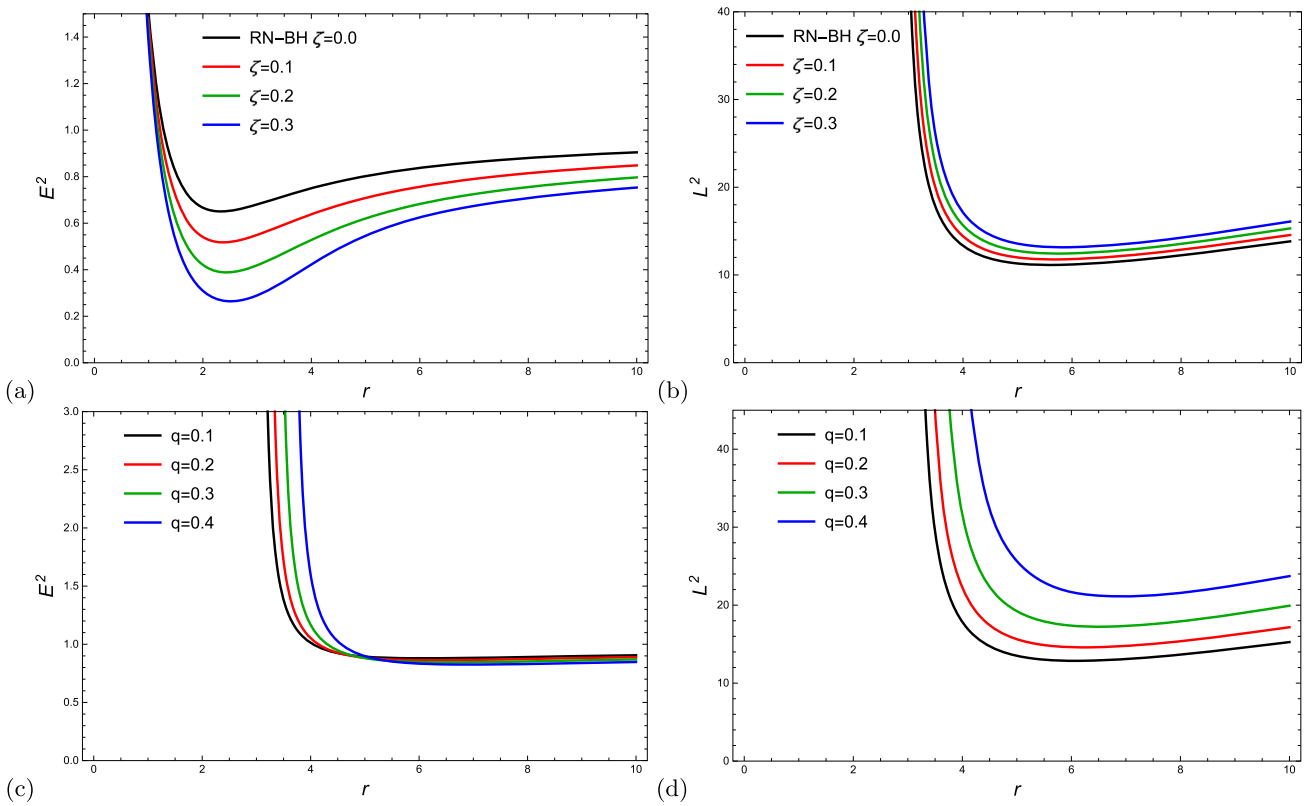

Fig. 6 The profile of energy illustrated in left plots while in right plots angular momentum is depicted along r for numerous values of NED parameters ζ and q

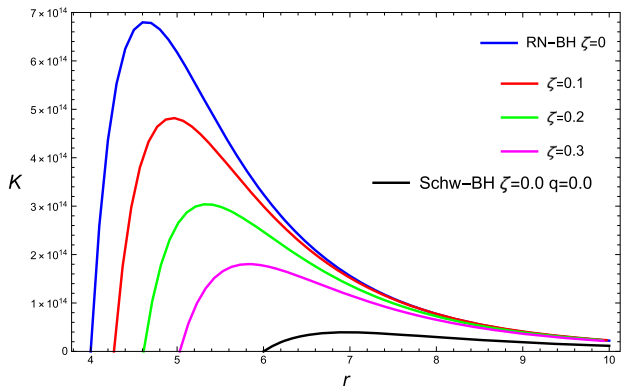

Fig. 7 The profile of energy flux K along r, for different value of ζ

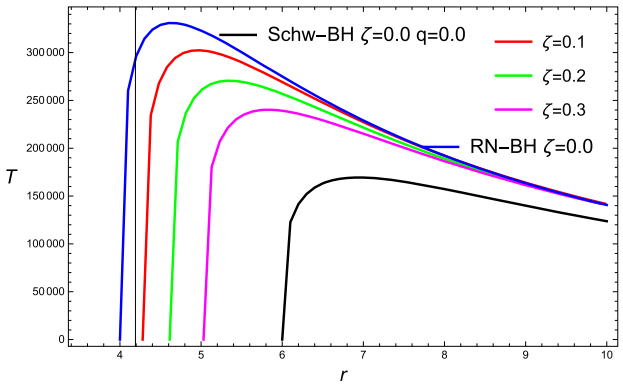

Fig. 8 The radiation temperature profile for various values of ζ

the parameter ζ grows, the flux energy of the accretion disc decreases.

5.2 Radiant temperature

It is speculated that the accretion disc is in thermal equilibrium, so the emission of radiation to the disc follows black body radiation principles. The Stefan-Boltzmann law, $K(r) = \sigma T^4$, established a relationship between energy flux and temperature. Here, σ represents the Stefan-Boltzmann constant. The disc temperature is evaluated through the utilization of the BH parameter ζ. In Fig. 8, we observe the temperature distribution on a disc for different values of ζ while keeping the parameter $q = 1$ fixed. It is observed that the disc temperature drops as the parameter ζ assumes progressively larger values.

5.3 Radiative efficiency

The emission of radiation produced by the transformation of gravitational energy arises together with the gradual inward spiraling of the material comprising the disc towards its central region. The specific energy within the ISCO radius can be used to figure out the radiative efficiency, which is the ability of the central entity to convert mass at rest into radiation

$$\eta = 1 - E_{isco}. \tag{101}$$

The numerical outcomes of ISCO, the photon sphere radius r_{ph}, the marginally bound orbit r_{mb}, the specific energy at ISCO denoted as E^2_{isco}, the specific angular momentum at ISCO indicated as L^2_{isco}, the specific angular velocity at ISCO referred to as Ω^2_{isco}, the specific angular momentum at ISCO symbolized as l^2_{isco}, the maximum energy flux and the maximum temperature distribution are presented in Table 1.

5.4 Epicyclic frequencies

In the presence of perturbations within the equatorial plane, when the particles move along a circular orbit, that will produce small oscillations in the vertical and radial directions. The radial and vertical epicyclic frequencies are determined from Eqs. (58) and (59). Since the expressions of these quantities are a little bit lengthy, we are not going to present them explicitly here. Instead, we calculate them numerically and presented the results in Fig. 9. In Fig. 9, the profile of radial epicyclic frequency Ω_r can be examined along the dimensionless radial coordinate r for numerous values of NED ζ and charge q of BH. In the left panel, we observed that the radial epicyclic frequency increases as the value of the NED parameter ζ increases. In the right panel, it can be easily seen that as the value of the electric charge q increases, the radial epicyclic frequency increases. This means that the orbits become more stable as the values of ζ and q increase because stronger oscillations lead to more stable orbits. So, the system has enhanced resistance to perturbations, which means that the orbits are less likely to become unstable. From the observed trend, we found that the increase in ζ and q enhances the stability of the orbits due to the increase in the radial epicyclic frequency.

The behavior of vertical epicyclic frequency Ω_θ along the dimensionless radial coordinate r for various values of NED ζ and charge q of BH is investigated in Fig. 10. In the left panel, we can see that the vertical epicyclic frequency increases as the value of the NED parameter ζ increases. The effect of electric charge q on vertical epicyclic frequency is represented in the right panel. It has been observed that in region $0 < r \leq 1.8$ the vertical epicyclic frequency decreases due to the increment of eclectic charge q, but for $1.8 < r \leq 3$ the vertical epicyclic frequency increases as the electric charge q increases. Also, from this trend, we have analyzed that the stability of the orbits is affected by ζ and electric q. The NED parameter ζ enhances stability by increasing the vertical epicyclic frequency. In the right panel of Fig. 10, we have concluded that orbits in the region $0 < r \leq 1.8$ become less stable with a higher charge q, while orbits in the region $1.8 < r \leq 3$ become more stable with a higher charge q.

6 Conclusions

We investigate the process of accretion and particle geodesic motion surrounding the Reissner–Nordström BH coupled with NED parameter ζ, in the equatorial plane. The stability and circular geodesics of their orbits have been investigated, examining the oscillations that arise from perturbations, the existence of unstable orbits, and ultimately enabling the construction of a fundamental formulation for understanding accretion flow near the BH. Furthermore, the dynamical parameters, effective potential, typical radius, specific energy, epicyclic frequencies, specific angular momentum, emission rate, and mass accretion rate of the BH are determined. By establishing the state function $p = k\rho$ for isothermal fluid, one can deduce the general solutions within the framework of a Reissner–Nordström BH coupled with (NED) parameter ζ.

The transformation of the loci of unstable and stable circular orbits is the obvious outcome of the impact of the NED parameter ζ on the effective potential, as observed in our investigations. As the parameter ζ is enhanced, the V_{eff} has associated decline, thereby allowing us to identify the precise location of the ISCO as depicted in Fig. 5a. The location of the radii, namely r_{isco}, r_{ph}, and r_{mb}, within this particular spacetime exhibits significant deviations from the Schwarzschild solutions. The numerical results of these radii presented in Table 1 for numerous values of NED parameter ζ. These radii are increasing functions with respect to the NED parameter ζ, that is, for large values of parameter ζ all these radii have gone away from the central mass. Since the inner edge of the accretion disc is indicated by r_{isco}, our findings exhibit that for large deviations, the disc will be extended away from the central mass.

As the NED parameter ζ grows, the energy decreases whereas angular momentum increases and one can observe from the energy diagram, the range of the bound orbit increases for large deviations. The increment of parameter ζ decreases the E_{isco} and increases the efficiency of the accretion disc. The radiation flux energy attains its maximum value in the vicinity of BH and then decreases. The energy flux radiation decreases with increasing the NED parameter ζ for small radii, but reverse behavior is observed for larger radii. So, the reliance on the NED parameter ζ is considerable in the vicinity of BH and weak in far from BH. Also, the same behavior is observed for the temperature.

Table 1 The numerical results are presented for $M = 1$, $q = 1$ and various values of BH parameter ζ

ζ	ISCO	r_{mb}	r_{ph}	E^2_{isco}	L^2_{isco}	Ω^2_{isco}	l^2_{isco}	$K_{max}(r)$	$T_{max}(r)$	η
0.1	4.269443	0.39838	1.06187	0.825474	9.5805	0.0102266	11.6061	4.82×10^{14}	2.94×10^5	0.091444
0.2	4.61245	0.41429	1.11347	0.810873	11.5838	0.0086997	14.2856	2.93×10^{14}	2.65×10^5	0.0995153
0.3	5.03015	0.42962	1.15514	0.799613	14.1013	0.0072621	17.6351	2.1×10^{14}	2.33×10^5	0.105789

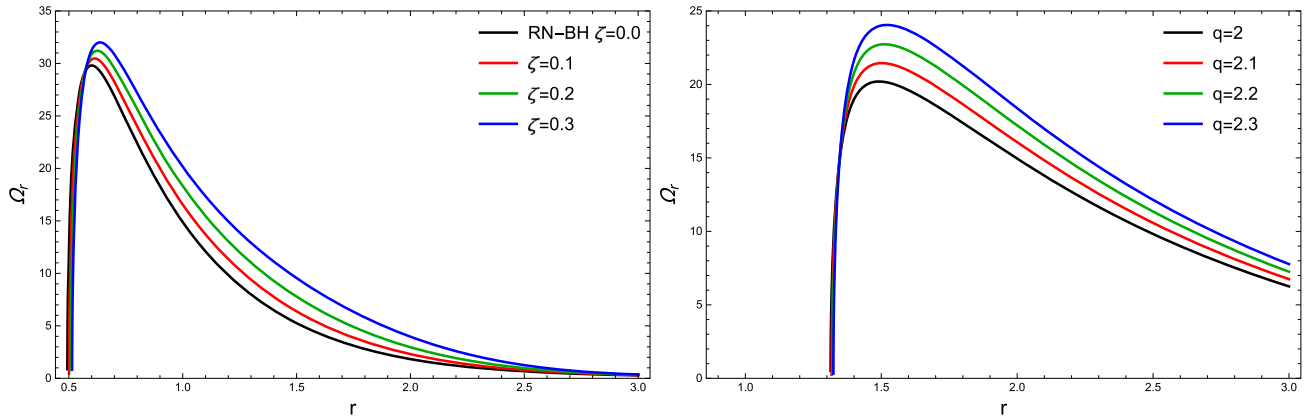

Fig. 9 The radial epicyclic frequencies depicted as a function of dimensionless r for altered values of NED parameter ζ in the left plot and electric charge q in right plot

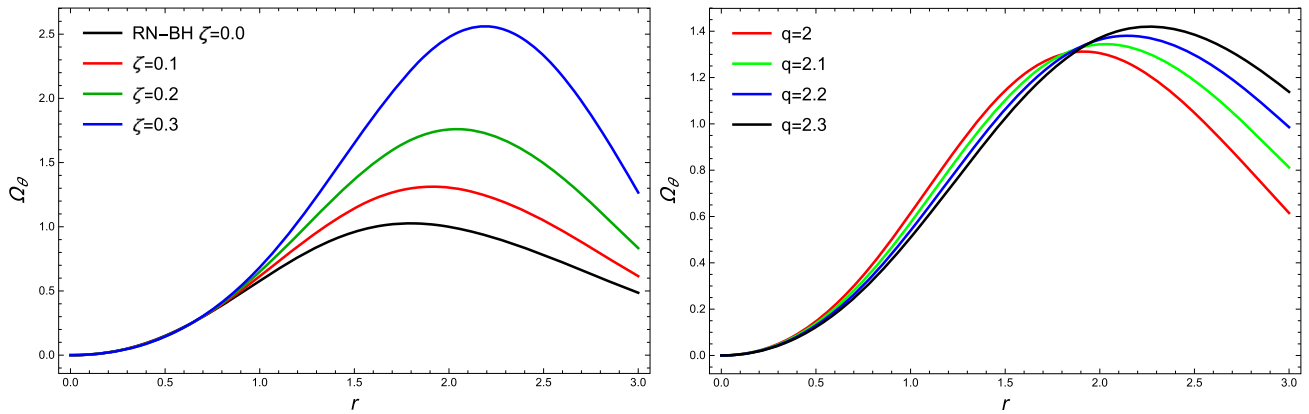

Fig. 10 The vertical epicyclic frequencies depicted as a function of r for altered values of NED parameter ζ in left plot and electric charge q in right plot

We examine the characteristics of the fluid particle density, radial velocity, and accretion processes by employing the state parameter $k = 0.5$ with considering isothermal fluid. It has been observed that the radial velocity attains maximum value in the vicinity of the BH for the parameters ζ and q but farthest from the BH fluid has no radial velocity. The accretion process happens when fluid traverses from the critical points its speed matches with sound speed. So prior to the critical point, the flow of the fluid has a subsonic regime, but the flow becomes supersonic as it crosses that point near the BH due to a strong gravitational field. Our key findings reveal that the velocity increases with increasing ζ and that the loci of the critical point shift away from the BH. As a result, infilling paretical speed matches with sound speed far from the central mass.

Upon examining the rate of accretion, we determined that its behavior extensively relies on fluid nature and BH parameters ζ and charge q. In the scenario of a normal fluid, the growth in mass accretion happens due to the immense gravitational field, and it has a maximum value near the BH. The rise in mass accretion occurs due to a positive deviation in the Schwarzschild BH scenario.

Finally, circular orbits with their properties and epicyclic frequencies are examined in this paper. The radial and vertical epicyclic frequencies are maximum in the vicinity of BH and the impact of the NED parameter ζ on radial and vertical

frequencies is considerable. The parameter ζ has remarkable effects on radial and vertical epicyclic frequencies in the vicinity of the BH, but as it moves away from the central mass, this effect becomes weak.

It is noteworthy that a non-spinning particle is taken into consideration in this study. If the spin of the particle exists, its orbit is significantly influenced by its spin. Moreover, the perfect fluid is assumed, and the magnetic field as well as the viscosity of the accretion disc are ignored for the sake of simplicity. So, the test particles motion is affected by these impacts, and as a consequence, they can affect the flux emission rate and structure of the accretion disc. In the future, we will investigate the motion of spinning particles and viscous fluid accretion subject to Reissner–Nordström BH coupled with a nonlinear electrodynamic field under the existence of a magmatic field.

Acknowledgements Tao Zhu is supported by the Zhejiang Provincial Natural Science Foundation of China under Grant no. LR21A050001 and LY20A050002, the National Key Research and Development Program of China Grant no. 2020YFC2201503, the National Natural Science Foundation of China under Grant no. 12275238 and no. 11675143, and the Fundamental Research Funds for the Provincial Universities of Zhejiang, China under Grants no. RF-A2019015. One of us (G. Abbas) really appreciates the fruitful discussion of Prof. Dr. M.H. Mazharimousavi about the review of nonlinear electrodynamics BH, who originally formulated the nonlinear electrodynamics BH.

Data Availability Statement Data will be made available on reasonable request. [Authors' comment: The current article is just theoretical article. We can share calculation on reasonable request.]

Code Availability Statement This manuscript has no associated code/software. [Authors' comment: Code/Software sharing not applicable to this article as no code/software was generated or analysed during the current study.]

Funded by SCOAP[3].

References

1. B.P. Abbott et al. [LIGO Scientific and Virgo], Observation of gravitational waves from a binary black hole merger. Phys. Rev. Lett. **116**(6), 061102 (2016). https://doi.org/10.1103/PhysRevLett.116.061102. arXiv:1602.03837 [gr-qc]
2. K. Akiyama et al. [Event Horizon Telescope], First M87 Event Horizon Telescope results. I. The shadow of the supermassive black hole. Astrophys. J. Lett. **875**, L1 (2019). https://doi.org/10.3847/2041-8213/ab0ec7. arXiv:1906.11238 [astro-ph.GA]
3. K. Akiyama et al. [Event Horizon Telescope], First M87 Event Horizon Telescope results. IV. Imaging the central supermassive black hole. Astrophys. J. Lett. **875**(1), L4 (2019). https://doi.org/10.3847/2041-8213/ab0e85. arXiv:1906.11241 [astro-ph.GA]
4. K. Akiyama et al. [Event Horizon Telescope], First Sagittarius A* Event Horizon Telescope results. I. The shadow of the supermassive black hole in the center of the Milky Way. Astrophys. J. Lett. **930**(2), L12 (2022). https://doi.org/10.3847/2041-8213/ac6674
5. I.G. Martnez, T. Shahbaz, J.C. Velazquez, *Accretion Processes in Astrophysics* (Cambridge University Press, Cambridge, 2014)
6. S.A. Kaplan, JETP **19**, 951 (1949)
7. L.D. Landau, E.M. Lifshitz, A. Lehbel, *The Classical Theory of Fields* (Pergamon, Oxford, 1993)
8. J.M. Bardeen, W.H. Press, S.A. Teukolsky, Rotating black holes: locally nonrotating frames, energy extraction, and scalar synchrotron radiation. Astrophys. J. **178**, 347 (1972)
9. M.P. Hobson, G.P. Efstathiou, A.N. Lasenby, *General Relativity: An Introduction for Physicists* (Cambridge University Press, New York, 2006), p.205221
10. I.D. Novikov, K.S. Thorne, in *Black Holes*. ed. by C. DeWitt, B.S. DeWitt (Gordon and Breach, New York, 1973), p.343
11. T. Johannsen, Inner accretion disk edges in a Kerr-like spacetime. Phys. Rev. D **87**(12), 124010 (2013). https://doi.org/10.1103/PhysRevD.87.124010. arXiv:1304.8106 [gr-qc]
12. T. Johannsen, D. Psaltis, A metric for rapidly spinning black holes suitable for strong-field tests of the no-hair theorem. Phys. Rev. D **83**, 124015 (2011). https://doi.org/10.1103/PhysRevD.83.124015. arXiv:1105.3191 [gr-qc]
13. A. Tursunov, Z. Stuchlík, M. Kološ, Circular orbits and related quasiharmonic oscillatory motion of charged particles around weakly magnetized rotating black holes. Phys. Rev. D **93**(8), 084012 (2016). https://doi.org/10.1103/PhysRevD.93.084012. arXiv:1603.07264 [gr-qc]
14. J.R. Isper, Astrophys. J. **435**, 767 (1994)
15. J.R. Isper, Astrophys. J. **458**, 508 (1994)
16. R.V. Wagoner, Relativistic diskoseismology. Phys. Rep. **311**, 259 (1999). arXiv:astro-ph/9805028
17. S. Kato, Basic properties of thin-disk oscillations. Publ. Astron. Soc. Jpn. **53**, 1 (2001)
18. M. Ortega-Rodriguez, A.S. Silbergleit, R.V. Wagoner, Normal modes of black hole accretion disks. Geophys. Astrophys. Fluid Dyn. **102**, 75–115 (2008). https://doi.org/10.1080/03091920701462130. arXiv:astro-ph/0611101
19. D.A. Tretyakova, Observational manifestations of black holes in the Horndeski gravity model. J. Exp. Theor. Phys. **125**(3), 403–409 (2017). https://doi.org/10.1134/S1063776117080118
20. K. Salahshoor, K. Nozari, Circular orbits and accretion process in a class of Horndeski/Galileon black holes. Eur. Phys. J. C **78**(6), 486 (2018). https://doi.org/10.1140/epjc/s10052-018-5946-2. arXiv:1806.08949 [gr-qc]
21. A. Ditta, G. Abbas, Circular orbits and accretion process near a regular phantom black hole. Gen. Relat. Gravit. **52**(8), 77 (2020). https://doi.org/10.1007/s10714-020-02724-9
22. G. Abbas, H. Rehman, M. Usama, T. Zhu, Accretion disc around black hole in Einstein-SU(N) non-linear sigma model. Eur. Phys. J. C **83**(5), 422 (2023). https://doi.org/10.1140/epjc/s10052-023-11600-0. arXiv:2303.02625 [astro-ph.HE]
23. D.A. Rasheed, Nonlinear electrodynamics: zeroth and first laws of black hole mechanics. arXiv:hep-th/9702087
24. N. Breton, Smarr's formula for black holes with non-linear electrodynamics. Gen. Relat. Gravit. **37**, 643–650 (2005). https://doi.org/10.1007/s10714-005-0051-x. arXiv:gr-qc/0405116
25. Y.-H. Wei, Energy and first law of thermodynamics for anti-de-Sitter black hole. Chin. Phys. B **19**, 090404 (2010)

26. M. Novello, E. Goulart, J.M. Salim, S.E. Perez Bergliaffa, Cosmological effects of nonlinear electrodynamics. Class. Quantum Gravity **24**, 3021–3036 (2007). https://doi.org/10.1088/0264-9381/24/11/015. arXiv:gr-qc/0610043
27. M. Novello, A.N. Araujo, J.M. Salim, Cyclic magnetic universe. Int. J. Mod. Phys. A **24**, 5639–5658 (2009). https://doi.org/10.1142/S0217751X09046321. arXiv:0802.1875 [astro-ph]
28. C.S. Camara, J.C. Carvalho, M.R. De Garcia Maia, Nonlinearity of electrodynamics as a source of matter creation in a flat FRW cosmology. Int. J. Mod. Phys. D **16**, 427–432 (2007). https://doi.org/10.1142/S0218271807010213
29. M. Novello, S.E. Perez Bergliaffa, J. Salim, Non-linear electrodynamics and the acceleration of the universe. Phys. Rev. D **69**, 127301 (2004). https://doi.org/10.1103/PhysRevD.69.127301. arXiv:astro-ph/0312093
30. M. Novello, S.E.P. Bergliaffa, Bouncing cosmologies. Phys. Rep. **463**, 127–213 (2008). https://doi.org/10.1016/j.physrep.2008.04.006. arXiv:0802.1634 [astro-ph]
31. V.A. De Lorenci, R. Klippert, M. Novello, J.M. Salim, Nonlinear electrodynamics and FRW cosmology. Phys. Rev. D **65**, 063501 (2002). https://doi.org/10.1103/PhysRevD.65.063501
32. K. Bronnikov, I. Dymnikova, E. Galaktionov, Multi-horizon spherically symmetric spacetimes with several scales of vacuum energy. Class. Quantum Gravity **29**, 095025 (2012). https://doi.org/10.1088/0264-9381/29/9/095025. arXiv:1204.0534 [gr-qc]
33. S.V. Bolokhov, K.A. Bronnikov, M.V. Skvortsova, Magnetic black universes and wormholes with a phantom scalar. Class. Quantum Gravity **29**, 245006 (2012). https://doi.org/10.1088/0264-9381/29/24/245006. arXiv:1208.4619 [gr-qc]
34. K.A. Bronnikov, K.A. Baleevskikh, M.V. Skvortsova, Wormholes with fluid sources: a no-go theorem and new examples. Phys. Rev. D **96**(12), 124039 (2017). https://doi.org/10.1103/PhysRevD.96.124039. arXiv:1708.02324 [gr-qc]
35. S. Nojiri, S.D. Odintsov, Regular multihorizon black holes in modified gravity with nonlinear electrodynamics. Phys. Rev. D **96**(10), 104008 (2017). https://doi.org/10.1103/PhysRevD.96.104008. arXiv:1708.05226 [hep-th]
36. C. Gao, Y. Lu, S. Yu, Y.G. Shen, Black hole and cosmos with multiple horizons and multiple singularities in vector–tensor theories. Phys. Rev. D **97**(10), 104013 (2018). https://doi.org/10.1103/PhysRevD.97.104013. arXiv:1711.00996 [gr-qc]
37. S.H. Mazharimousavi, Quark–antiquark confinement and nonlinear electrodynamics. Phys. Lett. B **841**, 137948 (2023). https://doi.org/10.1016/j.physletb.2023.137948. arXiv:2305.01048 [gr-qc]
38. R.H. Ali, B. Pourhassan, G. Mustafa, Quantum thermodynamics of the charged AdS black hole with nonlinear electrodynamics field. Chin. J. Phys. **88**, 768–785 (2024). https://doi.org/10.1016/j.cjph.2024.02.020. arXiv:2302.14641 [gr-qc]
39. E. Sucu, A. Övgün, The effect of quark–antiquark confinement on the deflection angle by the NED black hole. PDU **44**, 101446 (2024). https://doi.org/10.1016/j.dark.2024.101446. arXiv:2403.07044 [v1] [gr-qc]
40. E. Guendelman, Int. J. Mod. Phys. A **19**, 3255 (2004)
41. P. Gaete, E. Guendelman, Phys. Lett. B **640**, 201 (2006)
42. S. Kato, J. Fukue, S. Mineshige, *Black Hole Accretion Disks: Towards a New Paradigm* (Kyoto University Press, Kyoto, 2008)
43. D.F. Torres, Accretion disc onto a static nonbaryonic compact object. Nucl. Phys. B **626**, 377–394 (2002). https://doi.org/10.1016/S0550-3213(02)00038-X. arXiv:hep-ph/0201154
44. E. Babichev, V. Dokuchaev, Y. Eroshenko, The accretion of dark energy onto a black hole. J. Exp. Theor. Phys. **100**, 528–538 (2005). https://doi.org/10.1134/1.1901765. arXiv:astro-ph/0505618
45. E.O. Babichev, V.I. Dokuchaev, Y.N. Eroshenko, Black holes in the presence of dark energy. Phys. Usp. **56**, 1155–1175 (2013). https://doi.org/10.3367/UFNe.0183.201312a.1257. arXiv:1406.0841 [gr-qc]
46. M.A. Rodrigues, Accretion of nonminimally coupled scalar fields into black hole. Phys. Rev. D **80**, 104018 (2009). arXiv:0909.3033 [gr-qc]
47. S.K. Chakrabarti, *Theory of Transonic Astrophysical Flows* (World Scientific, Singapore, 1990)
48. M. Guo, P. Cheng Li, Innermost stable circular orbit and shadow of the 4D Einstein–Gauss–Bonnet black hole. Eur. Phys. J. C **80**, 588 (2020). https://doi.org/10.1140/epjc/s10052-020-8164-7. arXiv:2003.02523v3 [gr-qc]